A TIR forest reflectance and transmittance (FRT) model for directional temperatures with structural and thermal stratification

Zunjian Bian, Shengbiao Wu, Jean-Louis C. H. Roujean, Biao Cao, Hua Li, Gaofei Yin, Yongming Du, Qing Xiao, Qinhuo Liu

Remote Sensing of Environment xxx (xxxx) 112749

Contents lists available at ScienceDirect

Remote Sensing of Environment

journal homepage: www.elsevier.com/locate/rse

A TIR forest reflectance and transmittance (FRT) model for directional temperatures with structural and thermal stratification

Zunjian Bian [a,*], Shengbiao Wu [b], Jean-Louis Roujean [c], Biao Cao [a], Hua Li [a], Gaofei Yin [d], Yongming Du [a], Qing Xiao [a,e], Qinhuo Liu [a,e]

[a] State Key Laboratory of Remote Sensing Science, Aerospace Information Research Institute, Chinese Academy of Sciences, Beijing 100101, China
[b] School of Biological Sciences, The University of Hong Kong, Pokfulam, Hong Kong, China
[c] CESBIO - Centre d'Etudes Spatiales de la BIOsphère, CESBIO UMR 5126, 31401 Toulouse, France
[d] Faculty of Geosciences and Environmental Engineering, Southwest Jiaotong University, Chengdu 610031, China
[e] College of Resources and Environment, University of Chinese Academy of Sciences, Beijing 100049, China

ARTICLE INFO

Editor: Jing M. Chen

Keywords:
Forest
Land surface temperature
FRT model
Directional anisotropy

ABSTRACT

Land surface temperature (LST) is listed as an essential climate variable (ECV) and supports quantitative estimates of the energy budget while serving as a proxy for measuring the effects of climate change and extreme events. Forested areas are considered a major land unit impacted by temperature rise; therefore, thorough monitoring is mandatory. An accuracy assessment of the LST of forests must consider their directional anisotropy (DA). This latter can be well depicted by thermal infrared (TIR) radiative transfer models, but the problem is complex for forests because many of the shaded areas generate multiscale gradients of temperature. In this paper, we adapted a mature and widely used visible and near-infrared (VNIR) radiative transfer model called forest reflectance and transmittance (FRT) to enhance the characterization of the DA of forest temperature. In the FRT model, the vertical heterogeneity of the forest is quantified by using the discrete elements of multilayer scene components (i.e., the tree crown, trunk, understory vegetation, and soil), thus inferring vertical thermal gradients. The Planck function and spectral-invariant theory are considered to assess the thermal emissions of the scene components and their multiple scattering processes. The FRT model is validated using directional forest brightness temperatures (BT) measured from an unmanned aerial vehicle (UAV) and simulated by using the three-dimensional ray-tracing LESS (large-scale remote sensing data and image simulation framework over heterogeneous 3D scenes) model. The results show that FRT behaves reliably since the root mean square error (RMSE) is lower than 1.0 °C for UAV measurements obtained at 09:20 and 13:10 and with coefficients of determination (R^2) larger than 0.74 and 0.56, respectively; these results are better than the simulated results by existing models. Moreover, the comparison with ray-tracing simulations was also deemed satisfactory. According to the analysis, large variations in BT DAs may appear for different forests and seasonal changes staged by structural and thermal stratification, thus indicating the necessity of using the FRT model for complex and dynamic forest canopies.

1. Introduction

Land surface temperature (LST) is of vital interest in many disciplines, such as climate change, weather prediction and drought monitoring (Hu et al., 2020; Li et al., 2013a; Li et al., 2020). However, the remote sensing of thermal infrared (TIR) signals for retrieving LST is prone to angular dependence due to the specific illumination and viewing geometry of each pixel and the three-dimensional structure of the surface. Enhancing the characteristics of the directional anisotropies (DAs) of the brightness temperature (BT) is a prerequisite for analyzing and interpreting LST and upward longwave radiation (Bian et al., 2016; Verhoef et al., 2007). Hitherto, many TIR radiative transfer (RT) models had been proposed to support such an approach (e.g., the review by Cao et al., 2019). Although one-dimensional RT models, such as four-stream scattering by arbitrarily inclined leaves (4SAIL) and FR97, have been widely used because they require few inputs and do not require a thorough description of the canopy architecture (Francois et al., 1997; Verhoef et al., 2007), considering geometric optical (GO) models and

* Corresponding author.
E-mail address: bianzj@aircas.ac.cn (Z. Bian).

https://doi.org/10.1016/j.rse.2021.112749
Received 17 November 2020; Received in revised form 8 October 2021; Accepted 11 October 2021
0034-4257/

hybrid GO is still deemed necessary to treat most forested areas formed by heterogeneous canopies (Bian et al., 2018; Du et al., 2007; Kimes and Kirchner, 1982; Sobrino and Caselles, 1990; Yu et al., 2004).

Actually, a few research studies have been devoted to modeling the DAs of temperatures in forest canopies. The modified geometric projection (MGP) model proposed by Pinheiro et al. (2004) has been widely used, for example, in analyzing LST DAs and validating remote sensing LST products (Ermida et al., 2014; Ermida et al., 2018; Rasmussen et al., 2010). In this TIR model, four components, i.e., sunlit and shaded crown and sunlit and shaded soil, were considered. This is insufficient to handle the complexity of forest stands marked by a strong vertical stratification with specific attributes for the overstory with crown, the middle-layer trunk, the understory formed by a grass/shrub vegetation layer and finally the soil background. Moreover, some forest canopies may show seasonal trends, particularly deciduous canopies.

The BT of a whole forest and its DA signature is the result of the integration of the various thermal and structural characteristics of the diverse components. Balick and Hutchinson (1986) reported a significant trunk effect, approximately 3 °C per 10° change in viewing angle during a leafless period. A modified GO model was previously developed by Bian et al. (2020a) to analyze the tree trunk effect. Such a model is, however, limited to the treatment of dense canopies due to the assumption of homogeneity for the overstory tree leaves. A model that considers both forest trunks and leaf clumping for crowns instead of a random leaf distribution would accord more with the actual forest structure. Moreover, because of the large shape difference between overstory ellipsoidal-shaped/conical-shaped tree crowns and understory grass/shrubs, the vertical profile of vegetative attributes should be carefully considered, especially for sparse forests.

Complex forest structures have been the focus of numerous modeling efforts in the visible and near-infrared (VNIR) spectrum, such as the geometric optical radiative transfer (GORT) model, the forest reflectance and transmittance (FRT) model, the four-scale model and the analytical clumped two-stream (ACTS) model (Chen and Leblanc, 1997; Kuusk and Nilson, 2000; Ni-Meister et al., 2010; Ni et al., 1999). The TIR domain lacks equivalent models. The main difference between the VNIR and TIR models lies in the emission terms. Kimes et al. (1980) proposed a TIR model that highlights the gradients of temperature between the different layers of a crop canopy. Webster et al. (2018) reported that such variation can reach 5 °C based on three-dimensional observations from an unmanned aerial vehicle (UAV) system. The relative proportions of the different layers of a forest crown seen by a sensor vary with the viewing angle (Kimes et al., 1980). The consequence is the highlight of different material and structure; for example, the forest could appear as a different object according to how it is screened. In this regard, the approach consisting of using the average temperatures of sunlit and shaded crowns, as proposed by most TIR models, is unsatisfactory.

Departing from the above considerations, the aim of this study is to propose a TIR model for the directional BT of forests, including both structural and thermal stratification. Thermal emissions of components (i.e., the tree crown, trunk, understory vegetation, and soil) are introduced into the FRT model. A spectral invariant theory is adopted to account for the multiple scattering term using the geometry of different compounds. The FRT modeling framework is selected because it can depict the entire complex structure of the forest by reference to field experiments (Kuusk et al., 2014; Kuusk et al., 2008). The proposed model can be perceived as a thermal extension of the VNIR FRT model. The thermal version is validated using both measured and simulated datasets from a UAV-borne sensor and a three-dimensional ray-tracing model, respectively. In Section 2, the thermal version of the FRT model is described. In Section 3, UAV-based multiangle TIR observations and simulated datasets with different vegetation types are presented. In Section 4, the relevance of the FRT model is examined by comparing various simulation scenarios to analyze the effects of surface stratification. The limitations and potential applications of the approach are provided in Section 5. Section 6 summarizes the study and stresses some perspectives.

2. Methodology

2.1. Thermal version of the FRT model

In the TIR domain, the surface-leaving radiance is divided into two parts: the emission term from the target and the reflection term from the downward atmosphere. The top-of-canopy (TOC) radiance (L) can be expressed as follows:

$$L\left(\theta_s,\theta_v,\varphi\right)=\sum_j\left[\varepsilon_j\bullet f_j\left(\theta_s,\theta_v,\varphi,z\right)+\varepsilon_{m,j}\right]\bullet B_\lambda\left(T_{j,z}\right)+L_a^{\downarrow}\left(1-\varepsilon_e\right) \quad (1)$$

$$\varepsilon_e=\sum_j\left[\varepsilon_j\bullet f_j\left(\theta_s,\theta_v,\varphi,z\right)+\varepsilon_{m,j}\right] \quad (2)$$

where θ_s and θ_v are the solar zenith angle (SZA) and the view zenith angle (VZA), respectively; φ is the sensor-solar relative azimuth angle (RAA); T_j and ε_j are the temperature and the emissivity of the j component, respectively; f_j is the gap proportion of component j for the sensor; $\varepsilon_{m,j}$ is the emissivity of component j raised by the multiple scattering effects (this variable refers to the radiance emitted from component j and is scattered and reflected by other components to the sensor); z represents the height of a component; ε_e is the effective emissivity of the canopy as a whole; subsequently, $(1\text{-}\varepsilon_e)$ represents the canopy reflectance according to Kirchhoff's law; $\varepsilon_j \bullet f_j(\theta_s, \theta_v, \varphi, z) + \varepsilon_{m,j}$ can be viewed as the effective emissivity of the j component, and the effective emissivity of the canopy can be calculated as the sum of the effective emissivity of the components (Chen et al., 2004); $L_a^{\downarrow}$ is the downward effective radiance from the atmosphere; and B_λ is the Planck function that converts the component temperature to the thermal radiance with wavelength λ. In (1), the first part in the right panel represents the emitted radiance from the scene components, and the second part represents the reflected radiance from the downward atmosphere.

We adapted the FRT model to calculate the TOC radiance in (1). As shown in Fig. 1, the basic unit of the discrete tree crown in the FRT model is the volume element, thus the TOC radiance of the whole forest is calculated as the sum of contributions from all volume elements, where the directional/bidirectional gap probability consists of gaps between individual crowns and of within-crown gaps. To account for the stratification of the forest structure, we divided the whole forest canopy into four layers: the overstory tree crown, the middle-layer tree trunk, the understory vegetation, and the soil background. We further assumed sublayers for the tree trunk, the understory vegetation, and the forest crown, like the temperature, could vary at different heights of the canopy. According to (1), assuming no atmosphere, the TOC directional radiance of a forest scene is calculated as the sum of the direct emission component from the target component (i.e., $\varepsilon_j \bullet f_j(\theta_s, \theta_v, \varphi, z)$) and the multiple scattering component between the target and adjacent components (i.e., $\varepsilon_{m,j}$). Compared to VNIR, shaded components contribute more to the signal in the thermal spectrum as they emit. Thus, the sunlit and shaded areas in each layer are separated components. Although different tree species can be simulated by the FRT model, the forest scene for only a tree species was analyzed in this study because the overall objective here is to demonstrate the capability of the FRT model for modeling the thermal temperature of forests. For more details on the FRT model, we refer the reader to (Kuusk and Nilson, 2000).

2.2. Direct emission from components

It is assumed that each forest component is made of isotropic material for emission; for example, TIR radiometry drives the relative view-

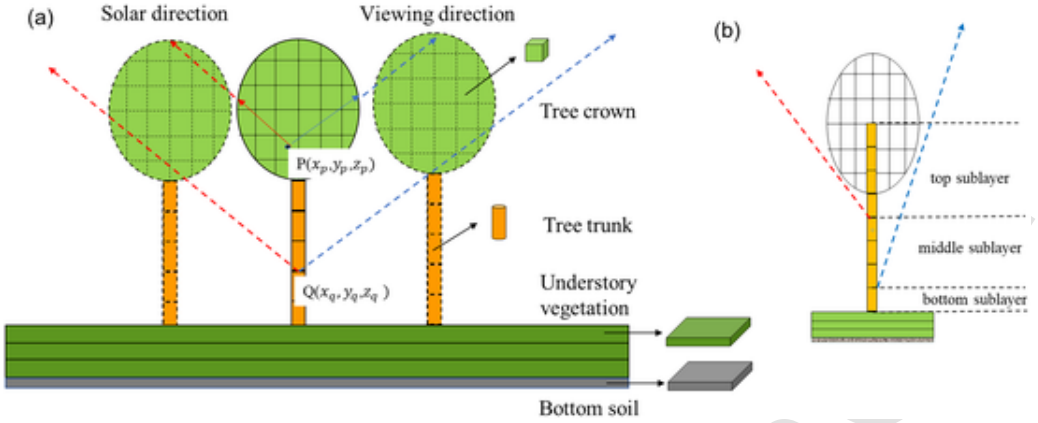

Fig. 1. (a) Sketch of the forest scene considered in this study. The tree canopies with dotted lines represent adjacent canopies depending on tree distribution and tree density. The blue and red lines represent view and solar directions, respectively; P and Q represent the target crown and trunk elements with the cartesian coordinates of (x_p, y_p, z_p) and (x_q, y_q, z_q), respectively. The dotted and solid lines represent the path between tree crowns and the within-crown path, respectively. (b) Three sublayers were divided for each tree trunk based on solar and viewing directions.

ing proportions of surface elements in the sensor field of view (FOV). Each component is modeled independently.

2.2.1. Tree crown

According to (Kuusk and Nilson, 2000), if the bidirectional gap probability of each volume element is known, the gap proportions of sunlit ($f_{c,s}$) and shaded ($f_{c,h}$) tree crowns can be calculated as follows:

$$f_{c,s}(r_s, r_v) = \sum f_{c,s,k}(r_s, r_v) \tag{3}$$

$$f_{c,h}(r_s, r_v) = \sum f_{c,h,k}(r_s, r_v) \tag{4}$$

$$f_{c,k}(r_v) = \lambda \int_{V_k} p_0(x, y, z, r_v) \bullet u_L \bullet G(\theta_v)/\mu_v \; dxdydz \tag{5}$$

$$f_{c,k,s}(r_s, r_v) = \lambda \int_{V_k} p_{00}(x, y, z, r_s, r_v) \bullet u_L \bullet G(\theta_v)/\mu_v \; dxdydz \tag{6}$$

$$f_{c,k,h}(r_s, r_v) = f_{c,k}(r_v) - f_{c,k,s}(r_s, r_v) \tag{7}$$

where $f_{c,k}$, $f_{c,s,k}$ and $f_{c,h,k}$ represent the gap proportions of the tree crown, sunlit crown and shaded crown in sublayer k, respectively; x, y and z represent the Cartesian coordinates of a volume element within the tree crown; V_k represents the spatial region indicating the envelope for a tree crown in sublayer k; r_s and r_v represent the solar and view directions, respectively; λ represents the tree density; p_0 represents the directional gap probability in a direction; p_{00} represents the bidirectional gap probability of the solar and view directions of r_s and r_v from an element; u_L represents the leaf area volume density; μ_v represents the cosine of the viewing direction; and G represents the fraction of foliage that is projected in the view or solar direction; this fraction is set as 0.5 for the spherical leaf inclination distribution function (LIDF). The direct emission in the TIR domain plays a major role and is analytically calculated by the interception probability of light by using $u_L \bullet G(\theta_v)/\mu_v$ $dxdydz$ based on a Lambertian assumption of emissivity. Worth outlining that it differs from the original parameterization in the VNIR FRT version, where the contribution of leaves in each volume to the TOC reflectance is expressed by the scattering area phase function of the canopy medium or the single-parameter Henyey-Greenstein phase function (Kuusk et al., 2014). The bidirectional gap probability p_{00} can be expressed as a product of two independent probabilities along the solar and view directions as follows:

$$p_{00}(x, y, z, r_s, r_v) = p_{ii}(x, y, z, r_s, r_v) \bullet p_{bb}(z', r_s, r_v) \tag{8}$$

where p_{ii} represents the bidirectional gap probability at the within-crown level, p_{bb} represents the bidirectional gap probability at the between-crown level, and z' represents the height of an intersection of light in the viewing or solar direction with the crown surface.

Because leaves within the tree crown are assumed to be homogeneous, p_{ii} depends mainly on the position of the volume element in the tree crown and on the leaf area volume density; therefore, p_{bb} is controlled mainly by the height z', tree density and leaf area volume density. In calculating the interception and the gap probabilities between contiguous tree crowns, the tree leaves located above a certain height z' and comprised of the spherical crown are clumped. Detailed information for calculating p_{ii} and p_{bb} can be found in Eqs. (29) and (30) in Appendix I.

2.2.2. Tree trunk

To calculate the thermal emissions of sunlit and shaded trunks, the entire trunk is considered because there is a large probability that the trunk within and under the tree crown can be seen by a sensor during a leaf-off period for a deciduous forest. The gap proportions of sunlit and shaded tree trunks can be expressed as follows:

$$f_t(r_v) = \lambda \int_{h_t} p_0'(z, r_v) \bullet d_t(z) \bullet \tan(r_v) \; dz \tag{9}$$

$$f_{t,s}(r_s, r_v) = \lambda \int_{h_t} p_{00}'(z, r_s, r_v) \bullet d_t(z) \bullet \tan(r_v) \bullet T(r_s, r_v) \; dz \tag{10}$$

$$f_{t,h}(r_s, r_v) = f_t(r_v) - f_{t,s}(r_s, r_v) \tag{11}$$

where f_t, $f_{t,s}$ and $f_{t,h}$ represent gap proportions of the trunk, sunlit trunk and shaded trunk, respectively; $p_0'(z, r_v)$ represents the directional gap probability in a direction r_v; $p_{00}'(z, r_s, r_v)$ represents the bidirectional gap probability between the solar and viewing directions of r_s and r_v from a sublayer at height z; d_t and h_t represent the diameter and height of the trunk, respectively; $T(r_s, r_v)$ represents the sun-view relative azimuth angle effect under the assumption that the trunk is cylindrical, being defined by $(\pi - \varphi)/\pi$. Despite the similar physical meaning of p_{00}' to that in (6), there are differences in its calculation:

$$p_{00}'(z, r_s, r_v) = p_{ii}'(z, r_s, r_v) \bullet p_{bb}(z', r_s, r_v) \tag{12}$$

where p_{ii}' represents the bidirectional gap probability of a light ray traveling through the crown in the solar or viewing directions. Several studies have demonstrated the role of the tree trunk in the RT modeling of a forest canopy. A simple method proposed in (Nilson and Kuusk, 2004) and used here consisted of separating the geometric projections

onto the horizontal plane of the tree crown and the tree trunk. As shown in Fig. 1(b), the tree trunk was divided into three sublayers: the top sublayer of the trunk projected by the crown in both the solar and viewing directions, the middle sublayer of the trunk projected by the crown in one direction, and the bottom part of the trunk outside the crown projection region. Then, $p_{ii'}$ was calculated separately for each sublayer. p_{bb} represents the bidirectional gap probability due to neighboring tree crowns and trunks. If a photon from a trunk sublayer at height z does not penetrate the tree crown in any direction, z' is equal to z. When a photon can be intercepted by its own crown, z' becomes the height of the upward intersection of a direction line and the crown surface. When z decreases, $p_{ii'}$ increases in trend with $p_{ii'} = 1$ for the bottom part of the trunk, whereas p_{bb} decreases.

2.2.3. Understory vegetation and soil

Considering the vertical gradient of temperature that exists for a forest canopy, depicting the properties of the sublayer formed by the vegetation understory well is meaningful in regard to the multiple bouncing of photons with forest attributes. The gap proportions of sunlit and shaded understory vegetation were calculated as follows:

$$f_{v,s}\left(r_s, r_v\right) = \sum_k f_{v,k,s}\left(r_s, r_v\right) \tag{13}$$

$$f_{v,h}\left(r_s, r_v\right) = \sum_k f_{v,k,h}\left(r_s, r_v\right) \tag{14}$$

$$f_{v,k}\left(r_v\right) = p_b\left(z_k, r_v\right) \bullet LAI_k \bullet G\left(\theta_v\right)/\mu_v \tag{15}$$

$$f_{v,k,s}\left(r_s, r_v\right) = p_{bb}\left(z_k, r_s, r_v\right) \bullet LAI_k \bullet G\left(\theta_v\right)/\mu_v \tag{16}$$

$$f_{v,k,h}\left(r_s, r_v\right) = f_{v,k}\left(r_v\right) - f_{v,k,s}\left(r_s, r_v\right) \tag{17}$$

where $f_{v,\ s}$ and $f_{v,\ h}$ represent the gap proportions of sunlit and shaded understories formed by vegetation, respectively; k represents a sublayer in the vertical direction at height z_k; and LAI_k represents the leaf area index (LAI) of the sublayer. The gap proportions of sunlit ($f_{s,\ s}$) and shaded ($f_{s,\ h}$) soil can be expressed as follows:

$$f_{s,s}\left(r_s, r_v\right) = p_{bb}\left(z = 0, r_s, r_v\right) \tag{18}$$

$$f_{s,h}\left(r_s, r_v\right) = f_s\left(r_v\right) - f_{s,s}\left(r_s, r_v\right) \tag{19}$$

$$f_s\left(r_v\right) = p_b\left(z = 0, r_v\right) \tag{20}$$

2.3. Multiple scattering effect between components

In the original VNIR FRT model, the multiple scattering term was modeled based on the four-flux approximation RT theory. Herein, different components with their own structural characteristics are considered, and an algorithm based on spectral-invariant theory (Bian et al., 2020a) appears to be a good option. The equations for homogenous leaves and tree trunks are provided in (Cao et al., 2018) and (Bian et al., 2020a), respectively. Therefore, the multiple scattering effect for tree crowns is the main focus. In this thermal version, only a single scattering effect was considered, and the interactions associated with the tree crown were calculated as follows (Francois et al., 1997):

$$\varepsilon_{m,c} = i_c p_c \varepsilon_c\left(1 - \varepsilon_c\right) + i_c' \varepsilon_c\left(1 - \varepsilon_u\right)\left(1 - i_c\right) \tag{21}$$

$$\varepsilon_u = \varepsilon_t i_t' + \left(1 - i_t'\right)\varepsilon_v i_v' + \left(1 - i_t'\right)\varepsilon_s\left(1 - i_v'\right) \tag{22}$$

$$p_c = 1 - e_{u,c} - e_{d,c} \tag{23}$$

$$e_{u,c} = \frac{1}{i_c} \bullet \sum_0^n p_0\left(x, y, z, r_v\right) \bullet \lambda \bullet u_L \bullet G\left(\theta_v\right)/\mu_v$$

$$a_{u,c} \bullet 2\int_0^{\frac{\pi}{2}} p_0\left(x, y, z, r\right) cos\theta sin\theta d\theta \bullet dxdydz \tag{24}$$

$$e_{d,c} = \frac{1}{i_c} \bullet \sum_0^n p_0\left(x, y, z, r_v\right) \bullet \lambda \bullet u_L \bullet G\left(\theta_v\right)/\mu_v$$

$$a_{d,c} \bullet 2\int_0^{\frac{\pi}{2}} p_0\left(x, y, hc - z, r, r\right) cos\theta sin\theta d\theta \bullet dxdydz \tag{25}$$

where i_c and i_c' represent the probability of directional interception of a photon due to the tree crown and its hemispheric averaging value, respectively; p_c represents the recollision probability, which is defined as the probability that a photon scattered from a leaf or needle in the canopy interacts with the canopy again; i_t' and i_v' represent the hemisphere interception probability due to trunk and understory vegetation, respectively; ε_t, ε_v and ε_s represent the material emissivity of trunk, understory vegetation and soil, respectively; $a_{u,\ c}$ and $a_{d,\ c}$ represent the upward and downward probability, respectively, after a photon is intercepted; $e_{u,\ c}$ and $e_{d,\ c}$ represent the upward and downward escape probability, respectively, of a photon from the tree crown; ε_u represents the hemispheric effective emissivity of components below the tree crowns (these components are the trunk, understory vegetation and soil); and $(1 - \varepsilon_u)$ represents the reflectance. The first and second terms in the right part of (21) represent the radiance emitted from tree leaves but reflected by other tree leaves and lower components, respectively, to a sensor.

3. Dataset

3.1. Measured dataset

Although extended work was performed in this study and satisfactory evaluation results of the VNIR FRT model were obtained according to several previous studies (Kuusk et al., 2014; Kuusk et al., 2008), some modifications were adopted, and a test was necessary. In this paper, the thermal FRT model was evaluated using multiangle TIR observations from a UAV system.

3.1.1. Experimental site

The UAV-based TIR experiment was performed at Saihanba National Forest Park (42.38 N, 117.37 E) located in Chengde, Hebei, China, with the Inner Mongolian Plateau standing in the northwest. This park was established in 1993 and covers 27,300 ha of seminatural mixed deciduous–conifer forest. The most common tree species in Saihanba National Forest Park are larch, spruce, pine and birch. A two-layer forest canopy can be observed there: the overstory consisted of larch, and the understory was formed by young Scots pine (*Pinus sylvestris* L.). Saihanba National Forest Park is in the cold temperate monsoon climate zone and has an average annual temperature of 1.3 °C; the snow season in Saihanba lasts for approximately 7 months each year. Therefore, a leaf-off forest canopy exists for a long time with distinct stratification with different components, as shown in Fig. 2(a).

3.1.2. UAV multiangle protocol

UAV observations conducted on April 15, 2021 were used to evaluate the thermal FRT model. Eight tracks along 4 directions were designed, as shown in Fig. 2(b). There were two squares of routes with side lengths of 50.0 m, and 0°-180° and 90°-270° directions were performed first, followed by 45°-225° and 135°-315° directions. The UAV experiments were performed on Beijing Time at approximately 09:20 and 13:10. The SZA and solar azimuth angles (SAA) at 09:20 were approximately 49.0° and 118.5°, respectively; and the corresponding values at 13:10 were approximately 35.0° and 206.1°, respectively. During the UAV experiment, the weather was clear.

Observations with different viewing angles were obtained by a series of thermal images as the UAV flew over the study area. A UAV-borne lightweight TIR camera (forward-looking infrared (FLIR) TAU2) was used to obtain the TIR data. This thermal camera provides images with 640 × 480 pixels with a spectral window of 7.5–13.5 μm. The noise equivalent delta temperature (NedT) of thermal infrared camera was lower than 0.05 °C. The accuracy of the radiometric calibration from digital number to blackbody temperature was approximately 0.5 °C. A wide-angle lens (69° × 56°) was attached to the camera with a forward inclination angle of 25°. Therefore, the maximum VZA for

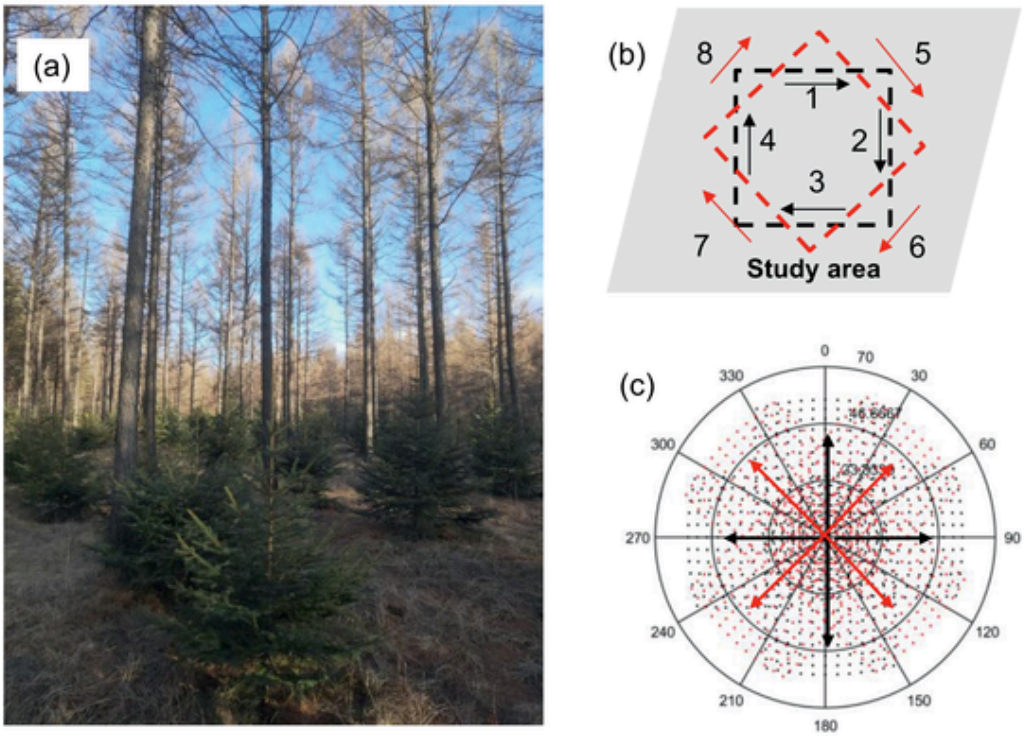

Fig. 2. A typical forest canopy (a) during leaf-fall period in Saihanba National Forest Park, in which overstory and understory canopies are larch and pine, correspondingly. (b) displays a sketch of the flight tracks and their sequence, and their corresponding viewing angles can be found in (c). In (c), the radii correspond to the azimuthal viewing directions, and the concentric circles indicate the zenithal viewing angles. Dots represent the field of view (FOV) of the camera during the UAV measurements.

each track can reach up to 55° in the flight direction and 28° in the cross-flight direction in theory. The designed viewing angles using 8 tracks can be found in Fig. 2(c). The actual viewing angles may vary due to the flight stability of the UAV. During the observations, the UAV height and speed were set to 50 m and 3 ms^{-1}, respectively.

3.1.3. UAV data preprocessing

The data preprocessing was performed as in (Bian et al., 2020a) including the radiometric calibration, the extraction of directional BTs and the atmospheric correction. The TIR camera was calibrated using a Blackbody EOI CES100 after measurements. In this process, the digital number in thermal images was transformed into brightness temperature, i.e., blackbody effective temperature. Directional BTs of the whole sample were extracted from all measured thermal images. The global positioning system (GPS) and position orientation system (POS) data were obtained synchronically for each image. Then, the viewing angle of each pixel in the images was calculated using the coordinates of the camera and each pixel. In this study, the GPS and POS data were refined by a structure from motion (SfM) algorithm in Agisoft Photoscan software (Webster et al., 2018), and the spatial resolution of the processed images was resampled to 0.10 m. Subsequently, a simple average method was applied to obtain effective directional observations of the whole sample based on Stefan Boltzmann theory because of the assumption of homogeneity (Lagouarde et al., 2010). It should be noted that the aggregated measurement was a statistical result. For a specific viewing angle, pixels in images corresponded to individual components or their combinations. The occurrence probability of components in these pixels was assumed equal to their visible proportions in this viewing angle. Detailed information can be found in (Lagouarde and Irvine, 2008; Lagouarde et al., 2004). After this extraction, directional BTs were stored with a 1° zenithal and azimuthal step. Worth mentioning is that a gentle smoothing was performed by averaging every BTs value over a running window 3 × 3 in θ_v and φ_v according to (Lagouarde et al., 2004). The atmospheric correction was performed with measured sky effective temperatures using a Fluke 561 thermometer with a VZA of 53° (Xiao et al., 2003). Directional canopy emissivities of this study area were estimated based on the 3D LESS model with average and standard deviation values of 0.986 and 0.001, respectively, for data with VZA range from 0° to 55° at a 5° step. Because the spectral response ranges between the Fluke thermometer (approximately 8 μm-14 μm) and Tau 2 thermometer were similar, and these two instruments were both calibrated using blackbody measurements, sky effective BTs were applied to eliminate atmospheric effect directly as follows:

$$T_{b,mea} = \sqrt[4]{T_{b,uav}^4 - \left(1 - \varepsilon_e\right) T_{b,sky}^4} \tag{26}$$

where $T_{b,\ mea}$ represents directional BTs after atmospheric correction, and $T_{b,\ uav}$ and $T_{b,\ sky}$ represent BTs from UAV-borne Tau 2 and field Fluke thermometers, respectively. ε_e is the canopy effective emissivity. This atmospheric correction was performed for each angle. Considering the temporal variability of BTs, the DAs were also calculated by using directional BTs minus the nadir BT.

3.1.4. Field measurements

In this study area, the shapes of overstory and understory crowns were measured by using laser rangefinder and tape. Heights of the overstory crown and its lowest live/death branches were measured, and then the tree crown vertical radius and trunk height were calculated with average values of 6.55 m and 12.05 m, respectively, and standard deviations of 1.81 m and 0.86 m, respectively. The height of understory crowns was obviously lower than that of overstory crowns with average and standard deviation values of 1.74 m and 0.14 m, respectively. Detailed information can be found in Table 1. The soil under the vegetation canopy was sandy loam, but dry grass existed sporadically during the period. The emissivity of the understory vegetation and soil was set to 0.978 and 0.955, respectively, according to (Arp and Phinney, 1980;

Table 1
Forest canopy structures for UAV-based data.

	Unit	First layer larch	Second layer pine
Height	m	18.6 ± 1.81	1.74 ± 0.14
Horizon radius	m	1.62 ± 0.35	0.52 ± 0.08
Vertical radius	m	6.55 ± 0.86	0.87 ± 0.07
h_t	m	12.05	–
d_t	m	0.31	–
LAI	–	0.51	0.48
λ	–	0.078	0.25
ε_c	–	0.930	0.978
ε_s	–	0.955	–
ε_t	–	0.930	–
2021-04-15 09:20			
T_{cs}, T_{ch}	℃	7.2, 4.3	6.4, 3.7
T_{ss}, T_{sh}	℃	17.7, 6.8	–
T_{ts}, T_{th}	℃	16.9, 4.1	–
2021-04-15 13:10			
T_{cs}, T_{ch}	℃	12.6, 11.3	11.2, 9.7
T_{ss}, T_{sh}	℃	23.8 12.9	–
T_{ts}, T_{th}	℃	21.9,10.7	–

Bian et al., 2018). The emissivity of tree trunks was set to 0.930, which was obtained from a spectral library in the DART model (Gastellu-Etchegorry et al., 2017). Because of the paucity of tree leaves, the emissivity of the tree crown was set to be the same as that of the tree trunks. LAIs were measured by a LAI 2200 Pant Canopy Analyzer. The LAI values shown in Table 1 were calculated from measurements. The LAIs for the whole canopy and for the crown/trunk canopy were measured separately. The effective LAI for the crown was calculated by the LAI value corresponding to the crown/trunk canopy minus the effective value of the trunk. The effective LAI for understory vegetation was calculated as the LAI value for the whole canopy minus that corresponding to the trunk/crown canopy. During the flights, the component temperatures of the sunlit/shaded leaves, soil and trunk were simultaneously measured using a FLIR S60 thermal camera; these temperatures were obtained by averaging the temperatures of pixels for each component. Because the actual temperatures of the components were used instead of their BTs in the considered models, a simple correction used in (Bian et al., 2016) was adopted in this paper. In the correction process of a component, the environmental radiance, i.e., emissions from sky and other components, was eliminated first, which contributions were determined by their hemispheric interception probability from the processed component multiplied by the reflectance of processed component. Then, the remaining radiance was divided by its material emissivity to obtain the actual temperature.

3.2. Simulated dataset

Forested areas form complex landscapes composed of diverse material. The present simulations considering different vegetation types, although these simulations may deviate somewhat from the true, are deemed sufficient to support a thorough analysis. The vertical stratification of the forest canopy in a TIR RT model can be divided into two aspects: 1) the heterogeneous structure of the canopy and 2) the temperature variations of the components. In this section, the structural heterogeneity was analyzed by comparing the simulated BTs for different forest canopies.

3.2.1. Scenes

The present approach differs from previous TIR models in that not only the four classical components, i.e., sunlit/shaded tree leaves and soil, are depicted, but also proposed here is a new design of the canopy where the tree trunk and understory vegetation in a forest are also accounted for. In addition to scenes with tree crowns, several scenes with homogeneous tree leaves were also generated, as shown in Table 2. A sketch map for these forest canopies can be found in Fig. 3. Fig. 3(a-d) represent canopies with homogeneous tree leaves, and Fig. 3(e-h) represent canopies with tree crowns. Among these scenes, S4 and S8, with

Table 2
Forest canopies with different components.

Case	Layers	Tree Crown	Homogenous Tree leaves	Tree Trunk	Understory vegetation	Soil
S1	2		√			√
S2	3		√		√	√
S3	3		√	√		√
S4	4		√	√	√	√
S5	2	√				√
S6	3	√			√	√
S7	3	√		√		√
S8	4	√		√	√	√

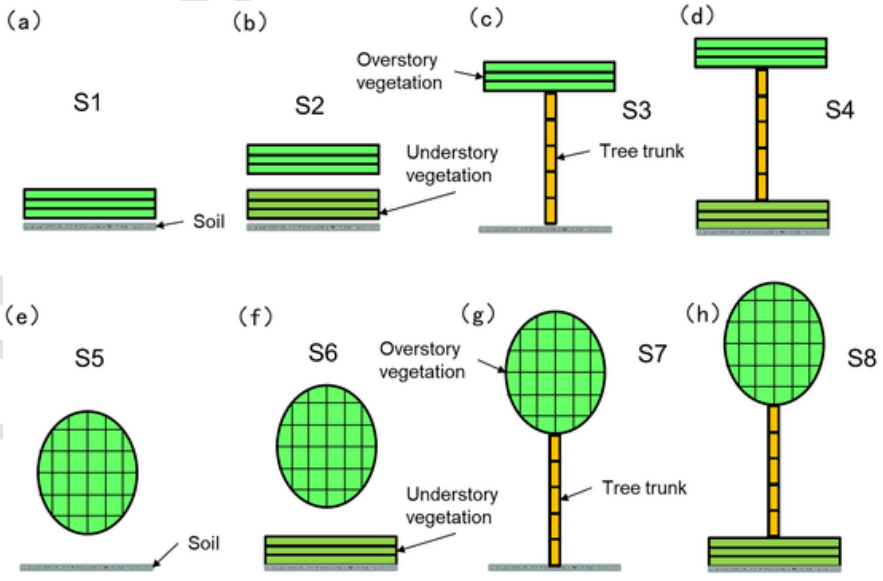

Fig. 3. A sketch map of forest canopies with different structures, in which (a-h) represent scenes (S1-S8) in Table 2.

eight components, can be viewed as actual cases for forests with homogeneous and crown-shaped tree canopies, respectively. S1 and S5 represent the most common cases in application with four components and were selected as the reference for comparison. In contrast to S1 and S5, understory vegetation was considered in S2 and S6, respectively, and tree trunks were considered in S3 and S7, respectively. The effects of the components, therefore, can be separately analyzed by comparing the simulated results for different forest canopies. These scenes were generated, on the one hand, because of the diversity of forests, such as rainforests, savannas, and plantations; on the other hand, some RT models were based on these assumptions to some extent. For example, S1 corresponded to the 4SAIL model (Verhoef et al., 2007), S5 corresponded to the MGP and UFR models (Bian et al., 2018; Pinheiro et al., 2004), and S3 corresponded to a thermal GO model (Bian et al., 2020a, 2020b). Simple models are generally preferred for solving problems. However, uncertainties may appear when a simple model is used for a complex forest canopy. Therefore, different scenes were designed for comparison.

3.2.2. Dataset

In most studies, tree leaves are usually a dominant factor for explaining the DAs of TOC BTs and for determining the contributions of the understory components. In S5-S8, only ellipsoid-shaped crowns were considered, with horizontal and vertical radii of 1.0 m and 3.0 m, respectively. A spherical LIDF was assumed for both overstory and understory leaves. Then, the overstory tree leaves were characterized by the leaf area index and tree density. The growth period of the forest was reflected by the overstory LAIs with values ranging from 0.3 to 3.0. The densities of the tree crowns were set to 500 ha^{-1}, 1000 ha^{-1} and 1500 ha^{-1} for sparse, medium and dense forest canopies, respectively. The same LAI, i.e., cumulative LAI of the overstory and understory leaves, was used. The LAI corresponded only to overstory leaves if there was no understory vegetation. Tree trunks can also affect the contributions of understory vegetation and soil. In this simulated dataset, the width and height of the tree trunks were set to 0.5 m and 10 m, respectively.

The key physical properties of the components are the emissivity and the temperature. The emissivity of the soil, trunks and leaves was set to 0.955, 0.930 and 0.975, respectively (Bian et al., 2020a). A component temperature profile measured at the Huailai remote sensing test site by using contact thermometers was considered: 33.5 °C/28.9 °C, 45.8 °C/29.4 °C and 47.8 °C/30.5 °C for sunlit/shaded tree crowns, bottom soil and tree trunks, respectively. The temperatures of sunlit and shaded understory vegetation were assumed to be 36.0 °C and 31.5 °C, respectively. This group of temperature components was used for all scenes in analyzing the structural heterogeneity of the forest canopy. The spectral wavelength of simulated TIR observations was set to 10.5 μm. The solar principal plane (SPP) was selected with VZAs ranging from −75° to 75° at a 5° step. Information on the simulated dataset can be found in Table 3.

Table 3
Inputs for simulated datasets.

Variable	Unit	Value/Range
Height	m	16
Horizon radius	m	1.0
Vertical radius	m	3.0
h_t	m	10.0
d_t	m	0.5
LAI	–	[0.3,3.0]
λ	–	0.05, 0.10, 0.15
ε_c	–	0.975
ε_s	–	0.955
ε_t	–	0.930
T_{cs}, T_{ch}	°C	33.5 °C/28.9 °C
T_{ss}, T_{sh}	°C	45.8 °C/29.4 °C
T_{ts}, T_{th}	°C	47.8 °C/30.5 °C
T_{vs}, T_{vh}	°C	36.0 °C/31.5 °C
SZA	°	30
VZA	°	[−75, 75]

4. Validation and analysis

4.1. Validation result

Directional BTs from the UAV were used to evaluate the proposed model. Simulated radiance by the model was transformed to BT based on the spectral response function of the Tau2 radiometer using a simple quadratic equation as follows:

$$T_{b,sim} = a\,L_{Tau,sim}^2 - b\,L_{Tau,sim} + c \tag{27}$$

$$L_{Tau,sim} = \int L_{\lambda,sim} f_\lambda d\lambda \tag{28}$$

where $T_{b,\,sim}$ represents the simulated BT used for comparison with UAV measurements; $L_{Tau,\,sim}$ represents the wide-band TIR radiance, which was calculated by spectral integration with spectral response function f_λ and model simulated $L_{\lambda,\,sim}$ at wavelength λ; and a, b and c are fitting coefficients with values of −0.3087, 12.8253 and −64.4630, respectively. The uncertainty of this expression is lower than 0.06 K for a temperature range from 270 K to 310 K. In the validation, the integration was performed with a spectral range from 7.5 μm to 15.0 μm with a step of 0.1 μm.

The polar plots for UAV-measured BTs at 09:20 and 13:10 can be found in Fig. 4(a) and 4(c), respectively. Angular variations in BTs were obvious in both panels, with maximum values larger than 3.0 °C. Fig. 4 (b) and 4(d) display FRT-simulated BTs at 09:20 and 13:10, respectively. The scattering results between the simulated and measured results can be found in Fig. 4(e) and 4(f). The FRT-simulated results accorded well with those measured by a UAV-borne sensor with RMSEs less than 0.85 °C and 0.96 °C at 09:20 and 13:10, respectively, and the corresponding coefficients of determination (R^2) were larger than 0.74 and 0.56. However, discrepancies still appeared: BTs with high values were underestimated, and those with low values were overestimated. The scattering results between the simulated and measured BT DAs can be found in Fig. 4(g) and 4(f). RMSEs and R^2 for BT DAs were similar to those for BTs. However, obvious overestimations were found in simulations for both 09:20 and 13:10, with biases of 0.83 °C and 0.69 °C, respectively. The overestimation of simulated BT DAs can be explained by the fact that the simulated nadir BT was obviously underestimated.

The evaluation results of other existing models can be found in Fig. 5 with statistical results shown in Table 4. For the results at 09:20, RMSEs of the thermal GO/trunk, MGP and SAIL models were larger, with values of 0.89 °C, 1.25 °C and 1.11 °C, respectively. Additionally, the R^2 of these models were lower, with values of 0.73, 0.56 and 0.59, respectively. Similar evaluation results can also be found for the data at 13:10. Clear differences in BTs between models appeared. Compared with the measurements, the simulated results by the thermal GO/trunk and SAIL models were underestimated; this underestimation can be explained by the underestimation of viewing fractions of components under tree leaves because large gaps between tree crowns were not considered. The MGP model can describe the tree crown shape in simulations, but the simulation results were overestimated because tree trunks and understory vegetation were ignored. Table 5 provides the comparison of BT DAs. Overestimations also appeared in simulations of these three models.

4.2. Comparison with the LESS model

The thermal version of the FRT model was also tested using a dataset simulated by a three-dimensional RT model, a large-scale re-

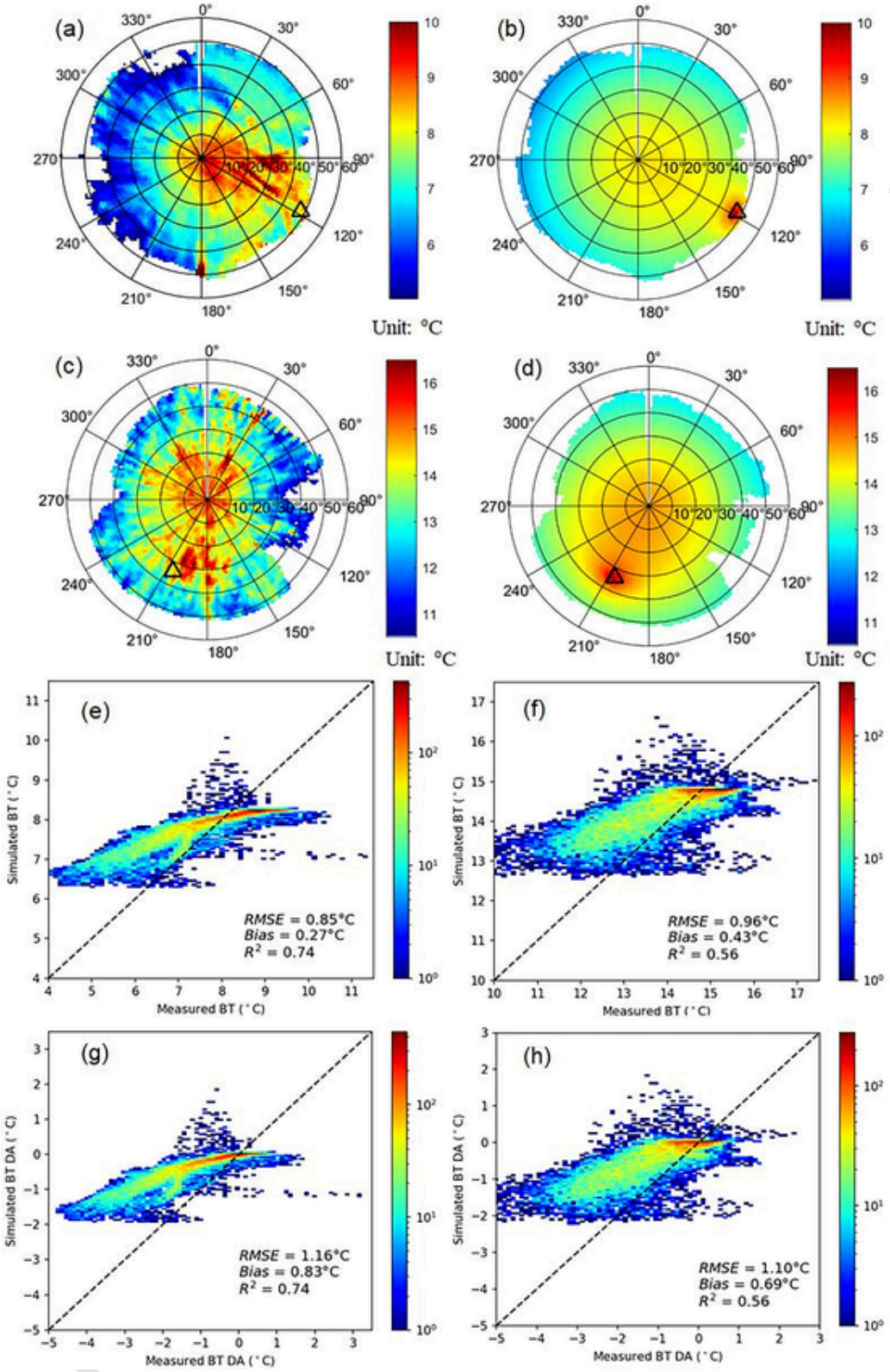

Fig. 4. Polar plots of UAV-measured (a, c) and FRT-simulated (b, d) BTs at 09:20 (a, b) and 13:10 (c, d), respectively. (e) and (f) display a comparison between UAV-measured and FRT-simulated BTs and (g) and (h) display BT DAs scattering plots.

mote sensing dataset and an image simulation framework over heterogeneous 3D scenes (LESS). The LESS model was used to allow a rapid simulation of LSTs in various complex forest canopies based on forward ray tracing and backward path tracing theories. The LESS model was selected because it was positively evaluated based on field measurements and comparisons with other three-dimensional models (Qi et al., 2019). Studies in (Cao et al., 2021) and (Qi et al., 2019) have shown LESS's performance is good for the red and NIR bands with RMSEs less than 0.0029 and 0.024, respectively. And the corresponding R^2 values are larger than 0.9. An intercomparison between LESS and SAIL model indi-

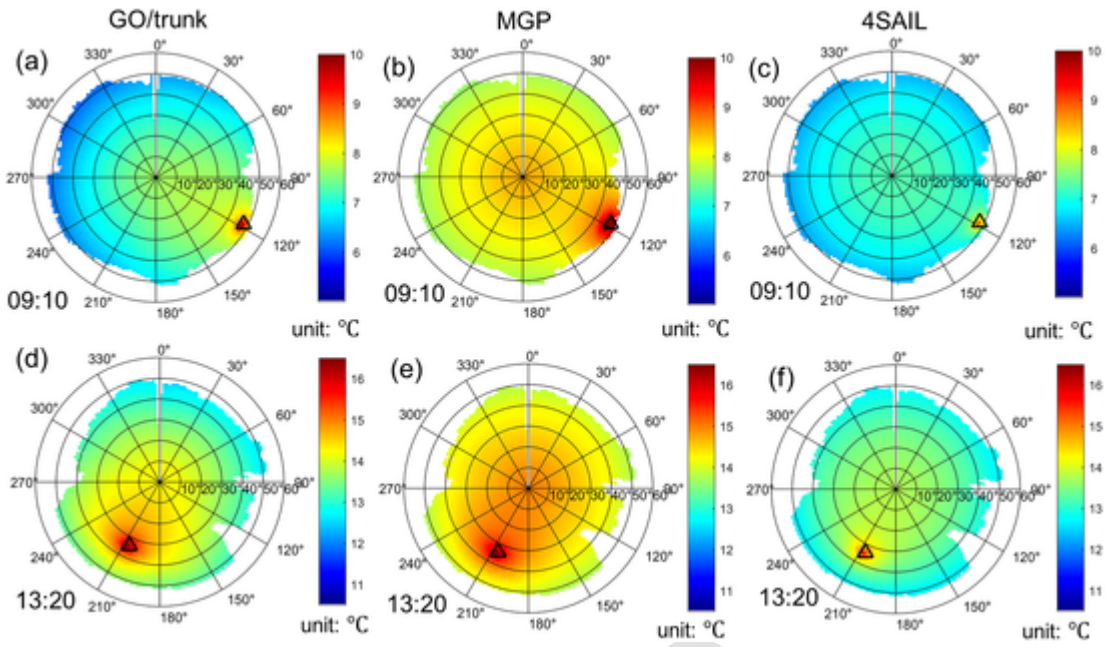

Fig. 5. Polar plots for BTs simulated by (a, d) GO/trunk, (b, e) MGP and (c, f) 4SAIL models. (a, b and c) for data at 09:20 and (d, e and f) for data at 13:10.

Table 4
Statistical results of BT simulated by models based on UAV measurements.

		Thermal FRT	GO/trunk	MGP	SAIL
09:20	RMSE (°C)	0.85	0.89	1.25	1.11
	R^2	0.74	0.73	0.56	0.59
	Bias (°C)	0.27	−0.19	0.75	−0.42
13:10	RMSE (°C)	0.96	0.98	1.29	1.04
	R^2	0.56	0.40	0.53	0.50
	Bias (°C)	0.43	0.16	0.84	−0.29

Table 5
Statistical results of BT DAs simulated by models based on UAV measurements.

		Thermal FRT	GO/trunk	MGP	SAIL
09:20	RMSE (°C)	1.16	1.30	1.43	1.50
	R^2	0.74	0.73	0.56	0.59
	Bias (°C)	0.83	0.98	1.01	1.09
13:10	RMSE (°C)	1.10	1.32	1.34	1.41
	R^2	0.56	0.40	0.53	0.50
	Bias (°C)	0.69	0.90	0.92	1.00

cates that the RMSE of temperatures is less than 0.1 °C. These validations prove a satisfactory performance of the LESS model in simulating the viewing proportions of components, the hot spot effect and the multiple scattering effect, which are vital factors in simulating BTs and their DAs.

Three-dimensional scenes were generated, as shown in Fig. 6(a) and 6(c), in which the overstory and understory leaves were described by triangular facets with a spherical LIDF. The overstory leaves were uniformly distributed within the tree crown, and those of the understory vegetation were randomly positioned slightly higher above the soil layer. A tree trunk is represented by six-sided cylinders. The temperatures of sunlit/shaded tree crowns, trunks, understory vegetation and bottom soil were 30.85 °C/28.85 °C, 42.85 °C/32.85 °C, 31.85 °C/29.85 °C and 41.85 °C/31.85 °C, respectively, i.e., 304 K/302 K, 316 K/306 K, 305 K/303 K, 315 K/305 K, respectively, in the 3D LESS model. Fig. 6(a) and 6(c) compare LESS-simulated and FRT-simulated BTs in the SPP in two cases with LAI values of the tree leaves of 0.5 and 2.5, respectively; and tree crown densities of 0.035 and 0.070, respectively. In these two figures, DAs with VZA and solar hotspot effects are obvious, and these DAs can be larger than 3.0 °C. The large R^2 (> 0.90) and low RMSE (< 0.50 °C) indicate that FRT-simulated BT DAs accorded well with those simulated by the LESS model. Fig. 6(b) and 6(d) compare BTs simulated by two models for the two aforementioned cases in hemispheric space with VZAs ranging from 0° to 75° with a 5° step size and RAAs ranging from 0° to 359° with a 30° step size. Satisfactory evaluation results were also obtained: RMSEs less than 0.45 °C and R^2 values larger than 0.94. The main difference in BTs between the two models was that the data around the solar hot spot domain were slightly overestimated by the FRT model.

4.3. The stratification of the forest canopy

In a natural environment, structural differences among forests are significant. Moreover, even within a forest, the canopy structure may vary according to the season. In this section, the effects of each component on BTs and their DAs are analyzed, and the simulated results are compared in terms of two aspects: 1) differences between forests and 2) seasonal variations within forests. The differences between forests were reflected by the stand density and separation of scene LAIs for the overstory and understory. Scene LAIs of 0.6, 2.0 and 4.0 were used to reflect different growth periods as seasonal changes.

4.3.1. Effects of components on BT DAs

Fig. 7(a) and 7(b) display simulated results of forest canopies with homogeneous and crown-clumped tree leaves, respectively. The LAIs of the overstory and understory were 1.5 and 0.5, respectively, and the tree crown density was 1000 ha^{-1}. The effect of the crown shape can be found by comparing simulated results for scenes with two types of tree leaves (i.e., S1-S4 and S5-S8). The BTs and the DAs of crown-clumped tree leaves were higher and larger, respectively, than those of homogeneous tree leaves in most cases because the gaps between crowns result in more viewing proportions of understory components in the FOV of a sensor. The trunk effect can be observed by comparing S1 and S3 or S5 and S7: a slight decrease caused by tree trunks was observed for data with VZAs lower than the SZA because in the FOV, the sunlit soil with a high temperature was replaced by shaded trunks and shadows of trunks with low temperatures. Compared to homogeneous tree leaves, a larger trunk effect appeared in scenes with crown-

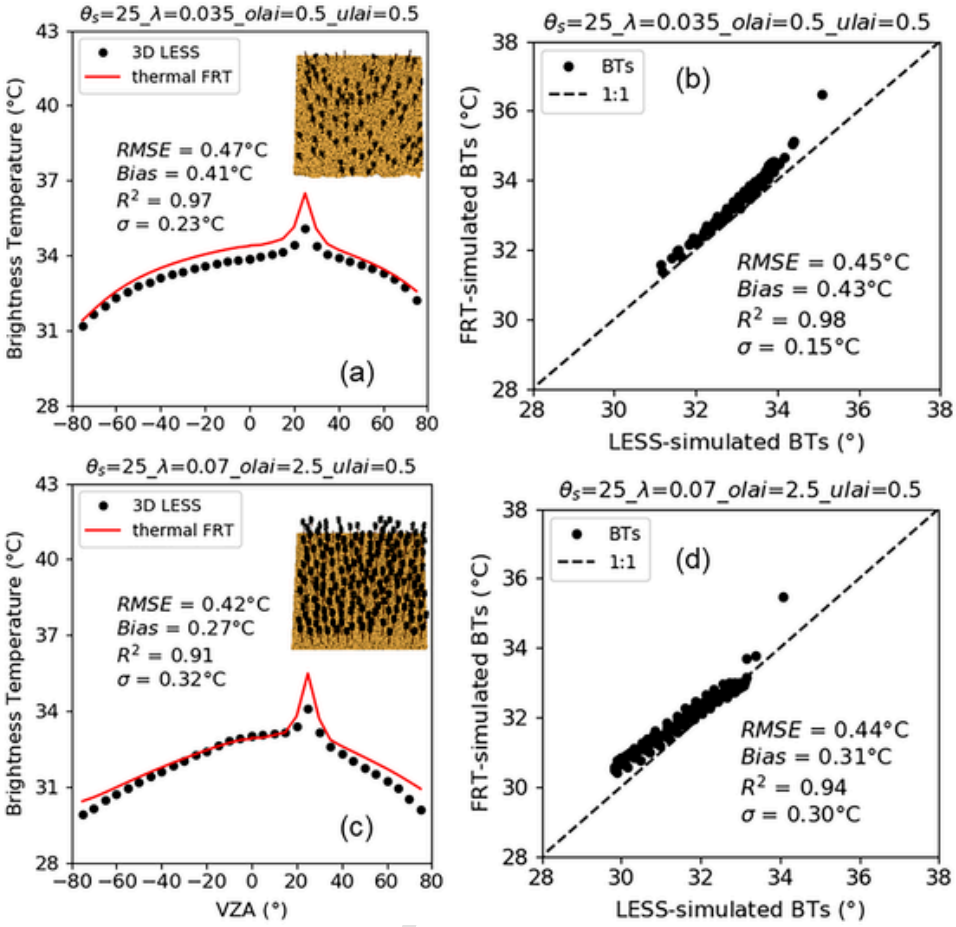

Fig. 6. Comparison between LESS-simulated and FRT-simulated BTs for cases with tree LAIs of (a, b) 0.5 and (c, d) 2.5 and stand densities of (a, b) 0.035 and (c, d) 0.070. (a, c) show the simulated results in the SPP, and (b, d) show the BTs in hemispheric space with VZAs from 0° to 75° at a 5° step and VAAs from 0° to 359° at a 30° step. θ_s, λ, *olai* and *ulai* represent the SZA, tree density, overstory and understory LAIs, respectively.

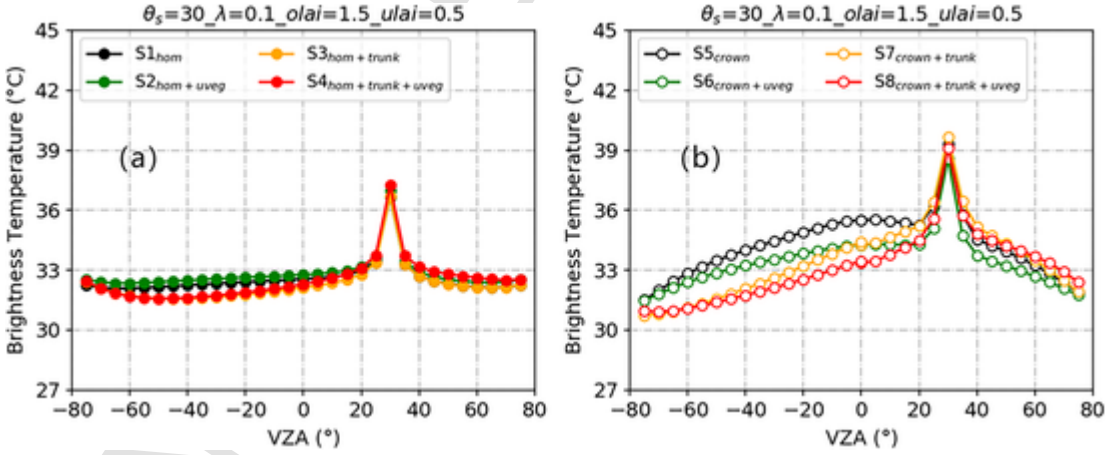

Fig. 7. Simulated results by thermal FRT in scenes with (a) homogeneous and (b) crown-clumping tree leaves. The overstory and understory LAIs were 1.5 and 0.5, respectively. The tree density was 0.1. Different colors represent vegetation canopies with different components, which are shown in Table 2.

clumping tree leaves because of larger viewing proportions of trunks and their shadows. For scenes with homogenous tree leaves, simulated results with understory vegetation were warmer than those without understory vegetation because the temperatures of the understory leaves were assumed to be slightly higher than those of the tree leaves. However, the understory vegetation caused BTs and their DAs to drop in forest scenes with crown-clumping tree leaves.

4.3.2. Differences in BT DAs due to different forests

As shown in Fig. 8, BTs and their DAs varied greatly, and as the stand density and rate of the understory LAI increased, the BT DAs increased. The former can be explained by the increasing trunk number, and the latter was due to the decreasing interception probability of the upper leaves in the viewing direction. Additionally, the impacts of the stand density and the rate of the understory LAI were slightly different: data with VZAs lower than SZA decreased in Fig. 8(b), whereas those

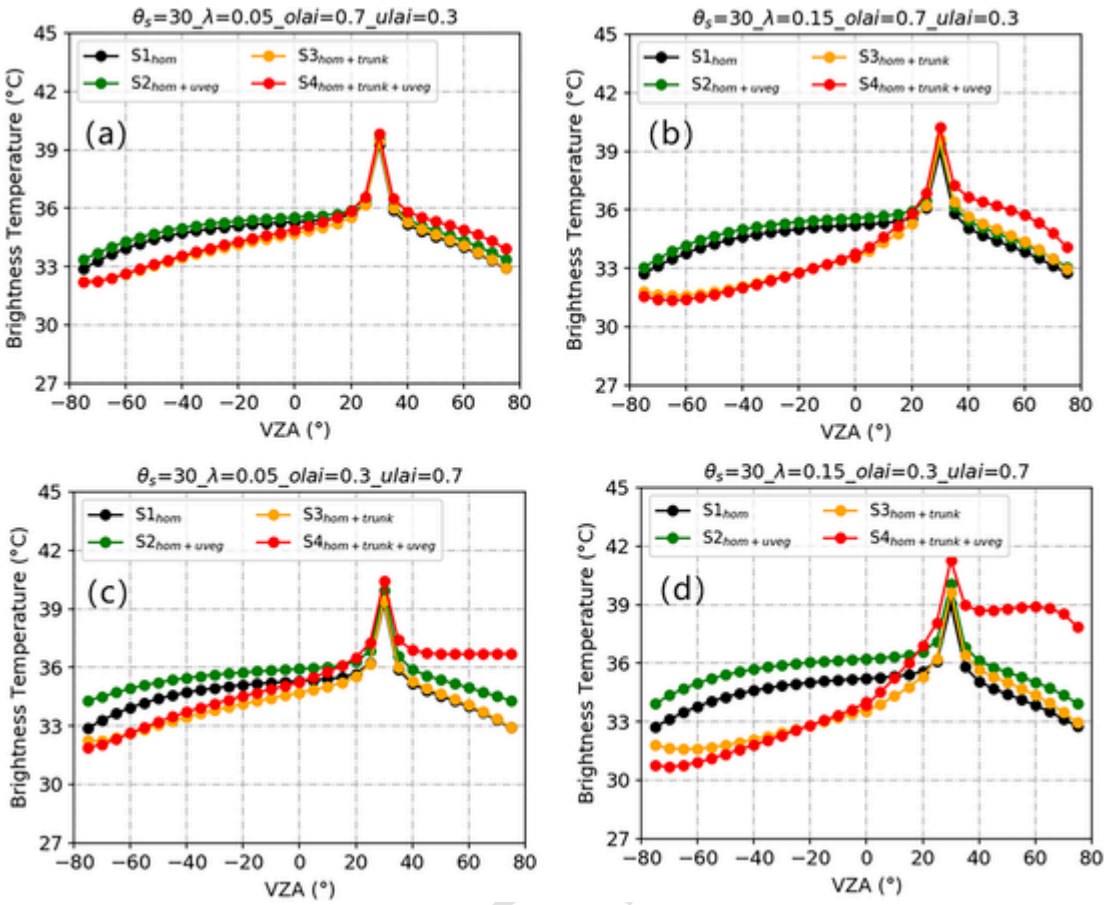

Fig. 8. Directional BTs in the SPP simulated for canopies with homogeneous tree leaves. The tree densities for (a, c) and (b, d) were 0.05 and 0.15, respectively; the LAIs of overstory and understory leaves for (a, b) were 0.7 and 0.3, respectively, and corresponding values for (c, d) were 0.3 and 0.7.

with VZAs larger than SZA increased in Fig. 8(c). The simulated results by S4 with VZAs larger than 30° were significantly warmer than those by other models. This can also be explained by the effect of trunks: with a small overstory canopy LAI and a large stand density, the viewing proportions of sunlit trunks increased. The BTs for S1 without tree trunks and understory vegetation were the same in these four panels, which can not indicate variations in BT DAs due to different forests.

Fig. 9 displays BTs simulated for different forests with crown-clumping tree leaves. When the stand density increased, BTs and their DAs decreased, contrary to the results for the cases with homogeneous tree leaves, particularly for S5 and S6. This is because the viewing proportion of the components under tree crowns decreased as the stand density increased. When the rate of understory LAI increased, the BT DAs also decreased because the clumping effect of the whole scene decreased when homogeneous understory vegetation played a considerable role. If the heterogeneity of the forest canopy had not been considered, these BT DAs would not have been shown correctly. When the stand density is quite high, BT DAs may vary slightly as the rate of the understory LAI increases.

4.3.3. Difference in BT DAs due to season

Fig. 10(a-c) display simulated results for forest canopies with homogeneous tree leaves. With seasonal changes, BTs and their DAs changed significantly, and these changes were mainly in the early growth period, with scene LAIs varying from 0.6 to 2.0 because as the scene LAI increased, the effect of tree trunk and understory vegetation decreased sharply. When there were few green leaves, the BTs and their DAs were similar between the two types of scenes with crown clumping and homogeneous tree leaves. As the scene LAI increased, the difference in BT between the two types of scenes increased significantly. Moreover, even if the scene LAI increased considerably, tree trunks and understory vegetation still played a role in TOC BTs and their DAs, as shown in Fig. 10(f).

5. Discussion

5.1. Model limitations and applications

In this paper, the VNIR FRT model was extended to the TIR domain to model TOC directional BTs for a complex forest with different components. Validation based on UAV data and comparison with a 3D model indicated that the thermal FRT model was reliable. Nevertheless, this modeling framework has several limitations: 1) in the FRT model, the branches in the tree crown are considered, but its shape characteristics are not well expressed; 2) when calculating multiple scattering effects between components, only a single-order term is considered, which can be identified as a compromise solution, and further analysis is required. Although the validation results indicate that the FRT model performed better than other existing models, the simulated results are unsatisfactory to some extent with respect to measurements. The two following factors explain these results. 1) Due to the existence of thermal inertia and the temporal variation in surface temperature during the UAV experiment, the hotspot effect is somewhat biased. 2) With respect to the temperature of each component, spatial variations resulting from RT and energy balance processes under certain conditions always appeared because the adjacent three-dimensional structure of the component is different. In the 13:10 case, the standard deviations of sunlit areas for tree leaves, trunks, understory leaves and soil are 0.43 °C, 0.41 °C, 1.76 °C, 0.68 °C, respectively; the standard deviations of shaded areas for tree leaves, trunks, understory leaves and soil are

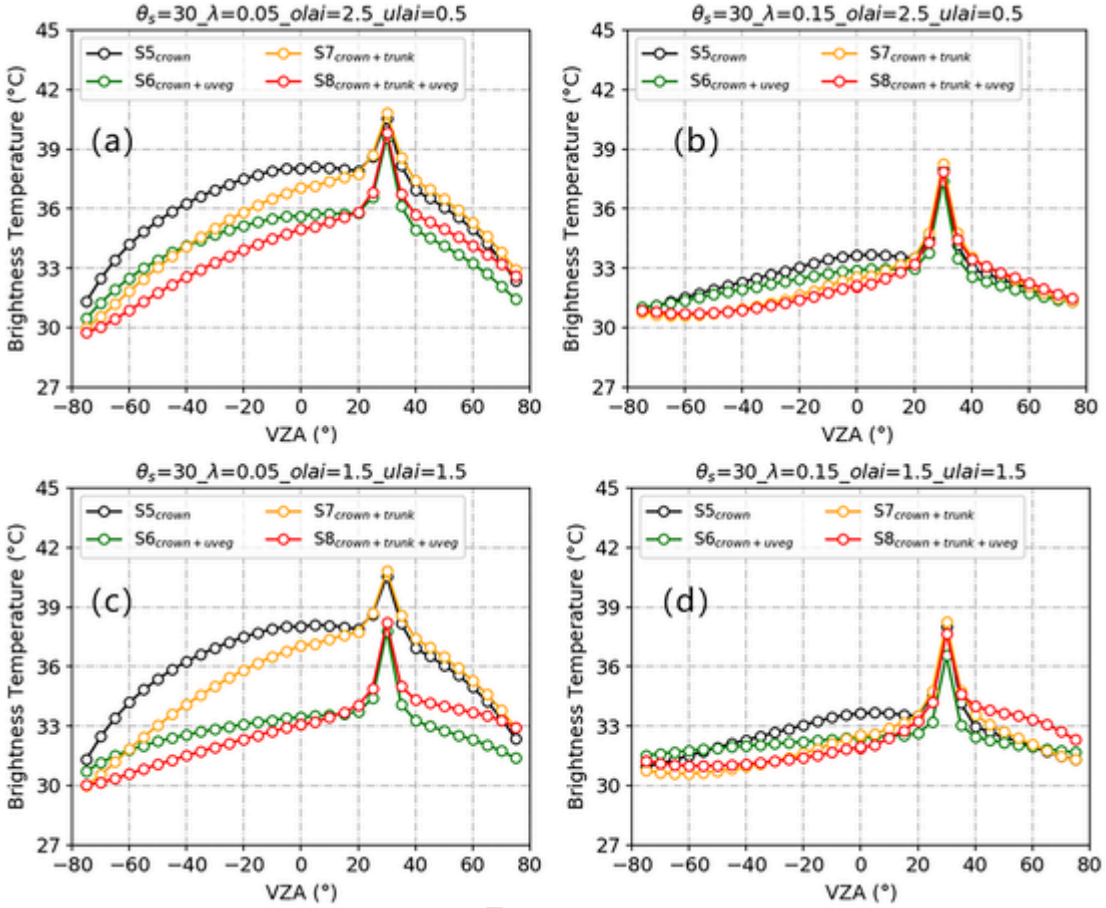

Fig. 9. Directional BTs in the SPP simulated for forest canopies with tree crown densities of (a, c) 0.05 and (b, d) 0.15; overstory and understory LAIs of 2.5 and 0.5 for (a, b), respectively; and 1.5 and 1.5 for (c, d), respectively; and spherical LIDF.

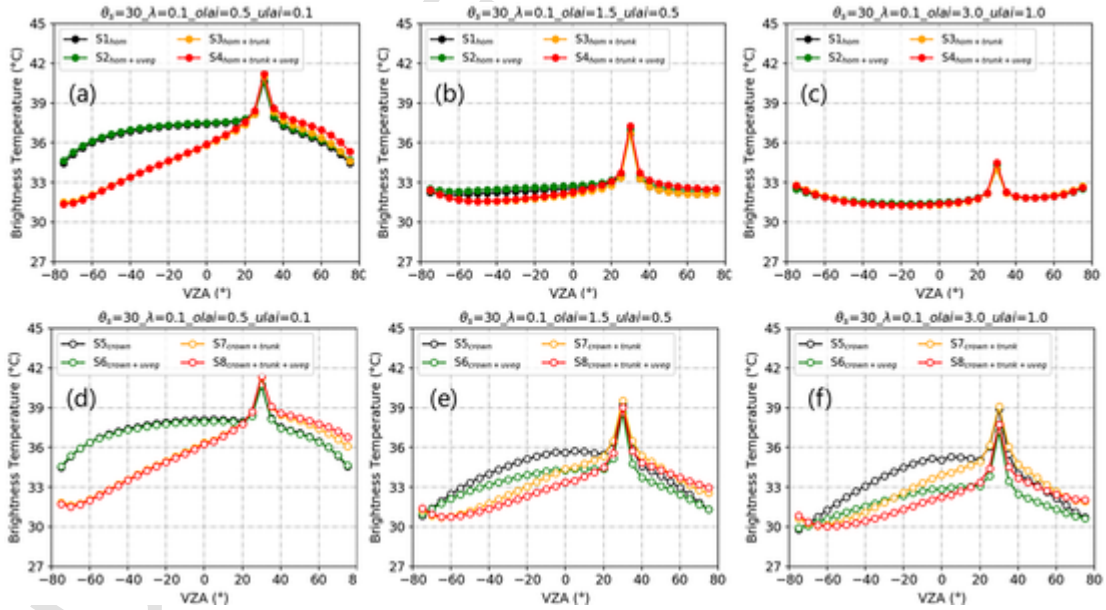

Fig. 10. Directional BTs in the SPP simulated for generated scenes with a tree density of 0.1, scene LAIs of (a, d) 0.6, (b, e) 2.0, and (c, f) 4.0, and spherical LIDF. (a)-(c) show the BTs for forest canopies with homogeneous tree leaves marked by solid circles. (d)-(f) show the BTs for forest canopies with tree crowns marked by hollow circles.

0.39 °C, 0.33 °C, 2.44 °C and 0.77 °C, respectively. Moreover, in some areas, particularly for the soil and trunk, the temperature may be much higher than its average value due to long-term solar exposure. However, the temperatures of components are considered homogeneous in the validation part, and discrepancies between simulations and measurements appeared.

The 3D model and the proposed model have their own advantages and disadvantages. Regarding the applicability of the model to the complex surface, the 3D model is the most appropriate. From the perspective of application, the proposed model performed better considering the analytical solution and the input requirement of statistical structural information rather than a detailed 3D scene, particularly for a large-scale scene. In addition, the proposed modeling strategy can be easily adopted and transplanted to surface comprehensive models for estimating thermal radiation in evapotranspiration or energy budget modules. A simple validation was also performed for the LESS model using UAV and field data. The RMSEs of BTs were lower than 0.78 °C and 0.96 °C for 09:20 and 13:10, respectively. This result is not significantly better than other analytical models, which may be explained by the fact that this validation was performed using statistical information such as the LAI and stand density as input rather than detailed 3D structural information, which affects the evaluation result of a 3D model inevitably.

5.2. Performance in directional emissivity

The focus of this paper is TOC BTs and their DAs. This thermal FRT model can also be used to calculate canopy emissivity according to (2). Fig. 11 displays the emissivity simulated by the proposed model for a forest scene with overstory and understory LAIs of 1.0 and 0.5, respectively, and emissivities of the soil, trunk and leaves of 0.955, 0.930 and 0.975, respectively. The emissivity results, indicated by cross symbols, from the 3D LESS model are shown for reference. The simulated results by the 4SAIL and MGP models are also provided for comparison, in which only tree leaves and understory soil are considered. FRT/SAIL and FRT/spectral-invariant represent the FRT framework with 4SAIL and spectral-invariant theories for the multiple scattering effect, respectively. The effective LAI, which is calculated in Appendix II, was used in FRT/SAIL. Compared to the results for FRT/SAIL, those for the FRT/spectral-invariant are closer to those yielded by the 3D model because the geometry of the components was accounted for in calculating the multiple scattering effect. There is no multiple scattering effect in the MGP model; therefore, the calculated canopy emissivity is somewhat lower, and its angular variation is totally determined by the viewing proportions of components. It should be noted that the results simulated by the 4SAIL model also agree well with the LESS-simulated results in this case. Nevertheless, due to the assumption of homogeneous tree leaves, the 4SAIL model is more suitable for homogeneous vegetation. Considering these comparison results, the emissivity simulated by the proposed model has potential for studying LST retrieval by using a split-window algorithm, which is known to be sensitive to surface emissivity (Li et al., 2013b; Li et al., 2014).

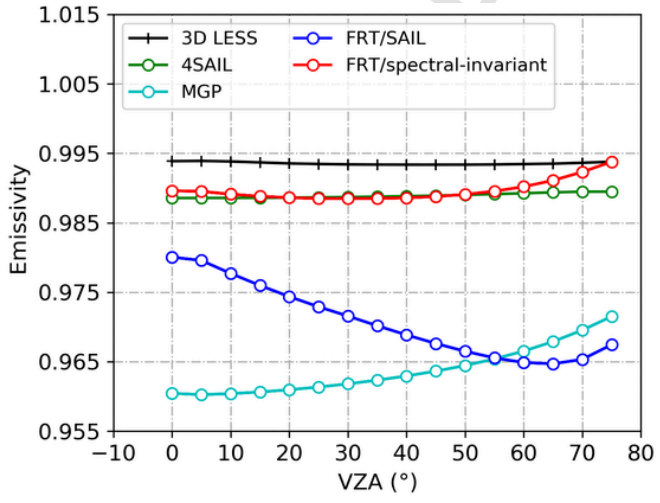

Fig. 11. Directional canopy emissivity for a forest scene with overstory and understory LAIs of 1.0 and 0.5, respectively, emissivities of the soil, trunk and leaves of 0.955, 0.930 and 0.975, horizontal and vertical crown radius of 1.0 m and 2.0 m and stand density of 0.1.

6. Conclusion

In a forest RT model, tree leaves and bottom soil are usually dominant factors for studying LSTs. However, the forest structure in nature is diverse and dynamic, and LSTs and their DAs are inevitably affected. A VNIR forest model, FRT, was therefore modified for TIR applications: the Planck function and spectral-invariant theory were introduced for the thermal emissions of components and the multiple scattering effect among components, respectively. On the basis of UAV-measured BTs at 09:20 and 13:10, the thermal FRT model was viewed as acceptable, with RMSEs of 0.85 °C and 0.96 °C and R^2 values of 0.74 and 0.56, respectively. Moreover, a comparison with a 3D ray-tracing model also indicated that the proposed model for simulating BTs was reliable, with RMSEs less than 0.5 °C and R^2 values larger than 0.90.

Based on the proposed model, a series of analyses was performed to investigate the effects of components on BTs and their DAs. BTs and their DAs may vary greatly for different forests and seasons. As the stand density and the understory LAI increase, BT DAs can show the opposite change between scenes with homogeneous and crown-clumping tree leaves. These phenomena indicate the necessity of considering the structural stratification of forest canopies. Because of the analytical solution of the thermal FRT model, we recommend that this proposed model be used to provide reference data for studying angular normalization algorithms of LST and component temperature inversion in forests.

Glossary

Abbreviations

RT Radiative transfer
GO Geometric optical
VNIR Visible and near-infrared
TIR Thermal infrared
LST Land surface temperature
BT Brightness temperature
DA Directional anisotropy
UAV Unmanned aerial vehicle
VZA Viewing zenith angle
SZA Solar zenith angle
RAA View-solar relative azimuth angle
SPP Solar principal plane
SAA Solar azimuth angle
FOV Field of view
TOC Top-of-canopy
GPS Global positioning system
POS Position orientation system
SfM Structure from motion
LAI Leaf area index
LIDF Leaf inclination distribution function
FRT Forest reflectance and transmittance
4SAIL Four-stream scattering by arbitrarily inclined leaves
SCOPE Soil canopy observation, photochemistry, and energy fluxes

LESS large-scale remote sensing data and image simulation framework over heterogeneous 3D scenes

Symbols

L Thermal radiance
θ_s, θ_v Solar and viewing zenith angle, respectively
φ View-solar relative azimuth angle
f_j Viewing proportion of component j
ε_j Material emissivity of component j
T_j Temperature of component j
$\varepsilon_{m,\,j}$ Multiple scattering effect of component j
$B(T_j)$ Planck function of temperature T_j
$L_a^{\downarrow}$ Downward effective radiance from the atmosphere
ε_e Effective emissivity of the whole canopy
z Height of an element of component
$f_{j,\,s}$, $f_{j,\,h}$ Gap proportions of sunlit and shaded component, respectively
p_{00} Bidirectional gap probability of the solar and viewing directions
p_i Bidirectional gap probability at the within-crown level
p_b Bidirectional gap probability at the between-crown level
cs, *ch* Subscript for sunlit and shaded crowns, respectively
ts, *th* Subscript for sunlit and shaded trunks, respectively
vs, *vh* Subscript for sunlit and shaded understory vegetation, respectively
ss, *sh* Subscript for sunlit and shaded soil, respectively
k Subscript for a sublayer in tree crown or trunk
x, *y*, *z* Coordinate for an element of a component
V_k Spatial region corresponding to the envelope for a tree crown in layer k
r_s, r_v Solar and viewing directions, respectively
λ Tree density
u_L Leaf area volume density
d_t, h_t Diameter and height of a trunk, respectively
$T(r_s, r_v)$ Solar-view relative azimuth angle effect because of the assumption that the trunk is cylindrical
G Fraction of foliage that is projected in the viewing or solar direction
i_c Directional probability of the interception of a photon due to the tree crown
i_c' Hemispheric averaging value of i_c
p_c Recollision probability
$e_{u,\,c}$,$e_{d,\,c}$ Upward and downward escape probability of a photon from the tree crown, respectively

Credit author statement

Zunjian Bian: Conceptualization, Methodology, Software, Writing - Original Draft; Shengbiao Wu and Jean-Louis Roujean: Conceptualization- Review; Gaofei Yin, Biao Cao, Hua Li and Yongming Du: Formal analysis and Methodology; Qing Xiao: Supervision; Qinhuo Liu: Supervision.

Uncited reference

Duffour et al., 2015

Declaration of Competing Interest

The authors declare that they have no known competing financial interests or personal relationships that could have appeared to influence the work reported in this paper.

Acknowledgments

The authors thank Dr. Kuusk, A. for providing the visible and near-infrared FRT model and suggestions and comments for TIR applications and all the scientists, engineers, and students who participated in the UAV experiment. This work was supported by the Chinese Natural Science Foundation Project (41901287, 41930111, 41871258), the National Key Research and Development Program of China under Grant 2018YFA0605503, a project funded by the China Postdoctoral Science Foundation, the Youth Innovation Promotion Association CAS under Grant 2020127, the "Future Star" Talent Plan of the Aerospace Information Research Institute of the Chinese Academy of Sciences under Grant Y920570Z1F, and the CAS President's International Fellowship for Visiting Scientists under Grant 2019DC0020.

Appendix I. Appendix

The bidirectional gap probability for a volume element

$$\begin{aligned} &p_{ii}\left(x,y,z,r_1,r_2\right)\\ &=a_i\left(s_1,\theta_1\right)a_i\left(s_2,\theta_2\right)\ C_{HSi}\left(s_1,s_2,\theta_1,\theta_2\right)\\ &a_i\left(s,\theta\right)=\exp\left[-su_L G\left(\theta\right)\right]\\ &C_{HSi}\left(s_1,s_2,\theta_1,\theta_2\right)\\ &=\exp\left[\sqrt{G\left(\theta_1\right)G\left(\theta_2\right)s_1s_2}\frac{\left(1-e^{-bs_{AB}}\right)}{bs_{AB}}u_L\right]\\ &s_{AB}=\sqrt{s_1^2+s_2^2-2s_1s_2cos\alpha} \end{aligned} \tag{29}$$

where $a_i(s, \theta)$ represents the proportion of gaps from the point to the crown surface with polar angle θ; C_{HSi} is the hot-spot correction factor, which characterizes the overlapping effect between the solar and viewing projections of within-crown leaves; s_1 and s_2 represent the path length from point (x, y, z) to the crown surface in the solar and viewing directions, respectively; α represents the solid angle between directions r_1 and r_2; and b is a hot-spot factor that was $16/(d_L\pi^2)$ for a spherical LIDF and $4/(d_L\pi)$ for a horizontal LIDF. p_{bb} characterizes the multiple shadowing effects between tree crowns, which were controlled by the tree crown upward from points $M_1(x_1, y_1, z_1)$ and $M_2(x_2, y_2, z_2)$ as follows:

$$\begin{aligned} &p_{bb}\left(z,r_1,r_2\right)\\ &=a_s\left(z_1,\theta_1\right)a_s\left(z_2,\theta_2\right)C_{HSb}\left(z_1,z_2,l_{12},r_1,r_2\right) \end{aligned} \tag{30}$$

$$C_{HSb}\left(z_1, z_2, l_{12}, r_1, r_2\right) = \exp\left[\lambda c S_c\left(z_1, z_2, l_{12}, r_1, r_1\right) p_0\right]$$

where $a_s(z, \theta)$ is the average proportion of gaps in the forest canopy at height z in direction θ; and C_{HSb} is the hot-spot correction factor, which characterizes between-crown shading in both the solar and viewing directions. The parameter c is introduced to account for deviations in the tree distribution pattern from a Poisson distribution; $S_c(z_1, z_2, l_{12}, r_1, r_1)$ is the area of the common part of the crown envelope projections in the solar and view directions, corresponding to heights z_1 and z_2 and horizontal distance l_{12}; and p_0 is the joint probability of gap occurrence within the tree crown. The gap probability $a_s(z, \theta_r)$ is calculated under the assumption of a binomial distribution of trees as follows:

$$\begin{aligned} a_s\left(z, \theta_r\right) &= \exp\left[-\lambda\left[c\left(z, \theta_r\right) S_{crown}\left(z, \theta_r\right) + S_{trunk}\left(z, \theta_r\right)\right]\right] \\ c\left(z, \theta_r\right) &= \ln\left[1-\left(1-a'\left(z, \theta_r\right)\left(1-ci\right)\right]\right/\left(1-ci\right) \end{aligned} \tag{31}$$

where S_{crown} is the area of the crown envelope projection at level z, S_{trunk} is the area of the trunk projection at level z, and $a'(z, \theta_r)$ is the gap probability in the crowns of trees in direction θ_r at level z. The function $a'(z, \theta_r)$ can be calculated as follows:

$$a'\left(z, \theta_r\right) = \exp\left[-u_L G\left(\theta_r\right) \frac{V(z)}{S_{crown}\cos\left(\theta_r\right)}\right] \tag{32}$$

Appendix II. Appendix

In (Tol et al., 2009), an analytical method was proposed and adopted for the multiple scattering effect in this multilayer forest canopy. Based on this method, the multiple scattering effect for sublayers of understory vegetation and soil was calculated directly based on the assumption of homogeneity. After a simple modification using an absolutely vertical LIDF, this method was applied to tree trunks. According to (Kuusk and Nilson, 2000), the multiple scattering effect for tree crowns was considered using the effective LAI (LAI_{eff}), which was calculated with the crown shape and clumping index as follows:

$$\begin{aligned} LAI_{eff} &= \frac{\kappa LAI + BAI}{\Omega_E} \\ \Omega_E &= \frac{\kappa LAI + BAI}{\cos\theta_0 \bullet \lambda \bullet S_{crown}\left(\theta_0\right) \bullet c\left(z=0, \theta_0\right)} \end{aligned} \tag{33}$$

where BAI represents the branch area index, κ represents the clumping coefficient of leaves/needles in a shoot, S_{crown} represents the crown projection in a direction, and Ω_E represents a clumping index for a canopy structure larger than a shoot. In the FRT modeling framework, θ_0 was set to 40°.

References

Arp, G.K., Phinney, D.E., 1980. Ecological variations in thermal infrared emissivity of vegetation. Environ. Exp. Bot. 20, 135–148.

Balick, L.K., Hutchinson, B.A., 1986. Directional thermal infrared exitance distributions from a leafless deciduous forest. Geosci. Remote Sens. IEEE Trans. GE- 24, 693–698.

Bian, Z., Xiao, Q., Cao, B., Du, Y., Li, H., Wang, H., Liu, Q., Liu, Q., 2016. Retrieval of leaf, sunlit soil, and shaded soil component temperatures using airborne thermal infrared multiangle observations. IEEE Trans. Geosci. Remote Sens. 54, 4660–4671.

Bian, Z., Cao, B., Li, H., Du, Y., Lagouarde, J.-P., Xiao, Q., Liu, Q., 2018. An analytical four-component directional brightness temperature model for crop and forest canopies. Remote Sens. Environ. 209, 731–746.

Bian, Z., Cao, B., Li, H., Du, Y., Fan, W., Xiao, Q., Liu, Q., 2020a. The effects of tree trunks on the directional emissivity and brightness temperatures of a leaf-off forest using a geometric optical model. IEEE Trans. Geosci. Remote Sens. 1–17.

Bian, Z., Roujean, J.L., Lagouarde, J.P., Cao, B., Li, H., Du, Y., Liu, Q., Xiao, Q., Liu, Q., 2020b. A semi-empirical approach for modeling the vegetation thermal infrared directional anisotropy of canopies based on using vegetation indices. ISPRS J. Photogramm. Remote Sens. 160, 136–148.

Cao, B., Guo, M., Fan, W., Xu, X., Peng, J., Ren, H., Du, Y., Hua, L., Bian, Z., Tian, H., 2018. A new directional canopy emissivity model based on spectral invariants. IEEE Trans. Geosci. Remote Sens. 1–16.

Cao, B., Liu, Q., Du, Y., Roujean, J.-L., Gastellu-Etchegorry, J.-P., Trigo, I.F., Zhan, W., Yu, Y., Cheng, J., Jacob, F., 2019. A review of earth surface thermal radiation directionality observing and modeling: historical development, current status and perspectives. Remote Sens. Environ. 232, 111304.

Cao, B., Qi, J., Chen, E., Xiao, Q., Liu, Q., Li, Z., 2021. Fine scale optical remote sensing experiment of mixed stand over complex terrain (FOREST) in the Genhe Reserve Area: objective, observation and a case study. Int. J. Digital Earth 14 (10), 1411–1432.

Chen, J.M., Leblanc, S.G., 1997. A four-scale bidirectional reflectance model based on canopy architecture. Geosci. Remote Sens. IEEE Trans. 35, 1316–1337.

Chen, L.F., Li, Z.L., Liu, Q.H., Chen, S., Tang, Y., Zhong, B., 2004. Definition of component effective emissivity for heterogeneous and non-isothermal surfaces and its approximate calculation. Int. J. Remote Sens. 25, 231–244.

Du, Y., Liu, Q., Chen, L., Liu, Q., Yu, T., 2007. Modeling directional brightness temperature of the winter wheat canopy at the ear stage. Geosci. Remote Sens. IEEE Trans. 45, 3721–3739.

Duffour, C., Olioso, A., Demarty, J., Van der Tol, C., Lagouarde, J.-P., 2015. An evaluation of SCOPE: A tool to simulate the directional anisotropy of satellite-measured surface temperatures. Remote Sens. Environ. 158, 362–375.

Ermida, S.L., Trigo, I.F., Dacamara, C.C., Göttsche, F.M., Olesen, F.S., Hulley, G., 2014. Validation of remotely sensed surface temperature over an oak woodland landscape — the problem of viewing and illumination geometries. Remote Sens. Environ. 148, 16–27.

Ermida, S.L., Trigo, I.F., DaCamara, C.C., Roujean, J.-L., 2018. Assessing the potential of parametric models to correct directional effects on local to global remotely sensed LST. Remote Sens. Environ. 209, 410–422.

Francois, C., Ottle, C., Prevot, L., 1997. Analytical parameterization of canopy directional emissivity and directional radiance in the thermal infrared. Application on the retrieval of soil and foliage temperatures using two directional measurements. Int. J. Remote Sens. 18, 2587–2621.

Gastellu-Etchegorry, J., Lauret, N., Yin, T., Landier, L., Kallel, A., Malenovský, Z., Bitar, A.A., Aval, J., Benhmida, S., Qi, J., Medjdoub, G., Guilleux, J., Chavanon, E., Cook, B., Morton, D., Chrysoulakis, N., Mitraka, Z., 2017. DART: recent advances in remote sensing data modeling with atmosphere, polarization, and chlorophyll fluorescence. IEEE J. Select. Topic Appl. Earth Observ. Remote Sens. 10, 2640–2649.

Hu, T., Renzullo, L.J., Dijk, A.I.J.M.V., He, J., Tian, S., Xu, Z., Zhou, J., Liu, T., Liu, Q., 2020. Monitoring agricultural drought in Australia using MTSAT-2 land surface temperature retrievals. Remote Sens. Environ. 236.

Kimes, D., Kirchner, J., 1982. Radiative transfer model for heterogeneous 3-D scenes. Appl. Opt. 21, 4119–4129.

Kimes, D.S., Idso, S.B., Pinter, P.J., Reginato, R.J., Jackson, R.D., 1980. View angle effects in the radiometric measurement of plant canopy temperatures. Remote Sens. Environ. 10, 273–284.

Kuusk, A., Nilson, T., 2000. A directional multispectral forest reflectance model. Remote Sens. Environ. 72, 244–252.

Kuusk, A., Nilson, T., Paas, M., Lang, M., Kuusk, J., 2008. Validation of the forest radiative transfer model FRT. Remote Sens. Environ. 112, 51–58.

Kuusk, A., Kuusk, J., Lang, M., 2014. Modeling directional forest reflectance with the hybrid type forest reflectance model FRT. Remote Sens. Environ. 149, 196–204.

Lagouarde, J.-P., Irvine, M., 2008. Directional anisotropy in thermal infrared measurements over Toulouse city Centre during the CAPITOUL measurement campaigns: first results. Meteorog. Atmos. Phys. 102, 173–185.

Lagouarde, J.-P., Moreau, P., Irvine, M., Bonnefond, J.-M., Voogt, J.A., Solliec, F., 2004. Airborne experimental measurements of the angular variations in surface temperature

over urban areas: case study of Marseille (France). Remote Sens. Environ. 93, 443–462.
Lagouarde, J.-P., Hénon, A., Kurz, B., Moreau, P., Irvine, M., Voogt, J., Mestayer, P., 2010. Modelling daytime thermal infrared directional anisotropy over Toulouse city Centre. Remote Sens. Environ. 114, 87–105.
Li, Z.-L., Wu, H., Wang, N., Qiu, S., Sobrino, J.A., Wan, Z., Tang, B.-H., Yan, G., 2013a. Land surface emissivity retrieval from satellite data. Int. J. Remote Sens. 34, 3084–3127.
Li, Z.L., Tang, B.H., Wu, H., Ren, H., Yan, G., Wan, Z., Trigo, I.F., Sobrino, J.A., 2013b. Satellite-derived land surface temperature: current status and perspectives. Remote Sens. Environ. 131, 14–37.
Li, H., Sun, D., Yu, Y., Wang, H., Liu, Y., Liu, Q., Du, Y., Wang, H., Cao, B., 2014. Evaluation of the VIIRS and MODIS LST products in an arid area of Northwest China. Remote Sens. Environ. 142, 111–121.
Li, H., Li, R., Yang, Y., Cao, B., Bian, Z., Hu, T., Du, Y., Sun, L., Liu, Q.J.I.T.O.G., Sensing, R., 2020. Temperature-Based and Radiance-Based Validation of the Collection 6 MYD11 and MYD21 Land Surface Temperature Products over Barren Surfaces in Northwestern China. 59. pp. 1794–1807.
Ni, W., Li, X., Woodcock, C.E., Caetano, M.R., Strahler, A.H., 1999. An analytical hybrid GORT model for bidirectional reflectance over discontinuous plant canopies. IEEE Trans. Geosci. Remote Sens. 37, 987–999.
Nilson, T., Kuusk, A., 2004. Improved algorithm for estimating canopy indices from gap fraction data in forest canopies. Agric. For. Meteorol. 124, 157–169.
Ni-Meister, W., Yang, W., Kiang, N.Y., 2010. A clumped-foliage canopy radiative transfer model for a global dynamic terrestrial ecosystem model. I: theory. Agric. For. Meteorol. 150, 881–894.
Pinheiro, A.C., Privette, J.L., Mahoney, R., Tucker, C.J., 2004. Directional effects in a daily AVHRR land surface temperature dataset over Africa. IEEE Trans. Geosci. Remote Sens. 42, 1941–1954.
Qi, J., Xie, D., Yin, T., Yan, G., Gastellu-Etchegorry, J.-P., Li, L., Zhang, W., Mu, X., Norford, L.K., 2019. LESS: LargE-scale remote sensing data and image simulation framework over heterogeneous 3D scenes. Remote Sens. Environ. 221, 695–706.
Rasmussen, M.O., Pinheiro, A.C., Proud, S.R., Sandholt, I., 2010. Modeling angular dependences in land surface temperatures from the SEVIRI instrument onboard the geostationary meteosat second generation satellites. IEEE Trans. Geosci. Remote Sens. 48, 3123–3133.
Sobrino, J., Caselles, V., 1990. Thermal infrared radiance model for interpreting the directional radiometric temperature of a vegetative surface. Remote Sens. Environ. 33, 193–199.
Tol, V.D.C., Verhoef, W., Timmermans, J., Verhoef, A., Su, Z., 2009. An integrated model of soil-canopy spectral radiances, photosynthesis, fluorescence, temperature and energy balance. Biogeosciences 6, 3109–3129.
Verhoef, W., Jia, L., Xiao, Q., Su, Z., 2007. Unified optical-thermal four-stream radiative transfer theory for homogeneous vegetation canopies. Geosci. Remote Sens. IEEE Trans. 45, 1808–1822.
Webster, C., Westoby, M., Rutter, N., Jonas, T., 2018. Three-dimensional thermal characterization of forest canopies using UAV photogrammetry. Remote Sens. Environ. 209, 835–847.
Xiao, Q., Liu, Q.H., Li, X.W., Chen, L.F., Xin, X.Z., 2003. A field measurement method of spectral emissivity and research on the feature of soil thermal infrared emissivity. J. Infr. Millimeter Waves 22, 373–378.
Yu, T., Gu, X., Tian, G., LeGrand, M., Baret, F., Hanocq, J.F., Bosseno, R., Zhang, Y., 2004. Modeling directional brightness temperature over a maize canopy in row structure. Geosci. Remote Sens. IEEE Trans. 42, 2290–2304.